Available online at www.sciencedirect.com
ScienceDirect
Journal of Power Sources 158 (2006) 1229–1239
JOURNAL OF POWER SOURCES
www.elsevier.com/locate/jpowsour

A two dimensional partial flooding model for PEMFC

Zhixiang Liu, Zongqiang Mao*, Cheng Wang

Institute of Nuclear and New Energy Technology (INET), Tsinghua University, Beijing 100084, PR China

Received 16 August 2005; received in revised form 14 October 2005; accepted 17 October 2005
Available online 28 November 2005

Abstract

Proton exchange membrane fuel cells (PEMFCs) have attracted much attention in these years. In PEMFCs, liquid/gas two-phase flow is a common phenomenon, which has great influence on fuel cell performance. However, the liquid water transport process has not been satisfactorily modeled yet. In this work, a two dimensional partial flooding model was developed, in which the pore size distribution of the gas diffusion layer (GDL) is taken into consideration in the explanation of fuel cell flooding for the first time. Liquid water produced is considered to flood a fraction of the GDL hydrophobic pores with diameter greater than the capillary condensation threshold diameter, and the unflooded pores will serve as passageway for gas transportation and the corresponding catalyst area is available for electrochemical reaction. Use this model, it is simple to explain membrane dehydration and electrode flooding. Different operation conditions have been studied with the model and the model polarization curves show reasonable accordance with the experimental results.

Keywords: Proton exchange membrane; Fuel cell; Model; Flooding

1. Introduction

Proton exchange membrane fuel cell (PEMFC), named by utilizing a proton conducting membrane as the electrolyte in the electrode sandwich, is one of the promising technologies for future electric vehicles, distributed power stations and portable power sources [1]. To date, most widely used electrolyte in PEMFCs is perfluorinated membrane, with excellent conductivity and durability, like well known Nafion® membrane from Dupont. However, as water is the proton carrier in this type of ionomer, which limits the operation temperature of fuel cell in a range where liquid water is stable, liquid/gas two-phase phenomenon is unavoidable and brings difficulty in water management. On the one hand, the membrane needs to be well hydrated to perform good proton conductivity, which requires humidification of reactants or taking measures to retain water in gas diffusion layers (GDLs) or membrane; on the other hand, the GDLs need to be flooding-proof to ensure free accesses for gaseous reactants transportation.

In the past years, many models were developed to study the transport and reaction phenomenon in fuel cells [2–8] and have been well reviewed by Yao et al. [9]. The pioneering models assumed that water was in gaseous state [2–4], which is not true for high current density or heavy humidification operation. In the past years, liquid water transport became one of the major concerns in fuel cell modeling and multi-phase models had been developed to study liquid/gas transport in porous GDL and flow channel by He et al. [10], Berning and Djilali [11], Kimble and Vanderborgh [12], You and Liu [13], Wang et al. [14]. Recently, there were some reports on flooding in catalyst layer [15,16]. These two-phase flow models assumed that both the liquid and gas phases were continuous, but no experimental picture confirmed this assumption [9]. Wang [17] classified the two-phase flow and transport modeling into two distinct approaches: continuum method and pore-scale method, most of the existing models belong to the former approach, where average porous media properties such as porosity, permeability and pore diameter were applied in the assumed homogenous diffusion layer. However, diffusivity of liquid water and gas varies quite much for different pore properties as shown in [18]. Pore-scale method for liquid transport modeling might be helpful in furthering the understanding of transport phenomena in fuel cells.

Till now, no model had taken the pore diameter distribution into consideration. However, GDL pore size distribution has greater influence on mass transport than total porosity in PEMFC as reported by Kong et al. [19]. The experimental results showed

* Corresponding author. Tel.: +86 10 627 84827; fax: +86 10 697 71150.
E-mail address: maozq@tsinghua.edu.cn (Z. Mao).

0378-7753/$ – see front matter © 2005 Elsevier B.V. All rights reserved.
doi:10.1016/j.jpowsour.2005.10.060

Nomenclature

a_w	activity of water
d	thickness (cm)
D	diffusing coefficient ($cm^2\ s^{-1}$)
f	unflooded pore area fraction
F	Faraday constant (96485 C mol^{-1})
i	average current density (A cm^{-2})
j	local current density (A cm^{-2})
j^0	exchange current density (A cm^{-2})
k	conversion coefficient (1/101325 atm Pa^{-1})
L	channel length (cm)
M_m	equivalent weight of dry membrane (g mol^{-1})
M_i	molar flow rate of species i (mol s^{-1})
n_d	electro-osmotic drag coefficient
N_i	flux of species i in y direction (mol s^{-1} cm^{-2})
p	gas pressure (atm)
P_{sat}	saturation water vapor pressure (atm)
r	radius of pores (cm)
r_0	average pore radius (cm)
R	gas constant (8.314 J mol^{-1} K^{-1})
R_m	membrane resistance (Ω cm)
T	temperature (K)
V	voltage (V)
w	channel width (cm)
X_i	molar fraction of species

Greek

α	net water drag coefficient from anode to cathode (H_2O/H^+)
α_a	anode transfer coefficient
α_c	cathode transfer coefficient
δ	surface tension of water (N cm^{-1})
ε	porosity of GDL
η	overpotential (V)
λ	water content in membrane (H_2O/SO_3^-)
θ	contact angle (°)
ρ_m	density of dry membrane (g cm^{-3})
σ_m	conductivity of membrane (S m^{-1})
χ	volume fraction of hydrophilic pores
ξ_i	coefficient
ω	coefficient in pore distribution function
ψ	pore distribution function

Subscripts

a	anode
c	cathode
h	hydrogen
m	membrane
n	nitrogen
o	oxygen
oc	open circuit
w	water

that macropores (5–20 μm) in diffusion layer are thought to prevent water flooding of electrode. In this paper, a two dimensional model was developed to account for the partial flooding phenomenon in fuel cells with GDL pore size distribution being considered for the first time.

2. Basic idea of the model

Carbon paper and carbon cloth are often applied as GDL in PEMFC after hydrophobic treatment with Teflon. During the treatment, Teflon is not possible to cover the carbon fibers uniformly, so there will be different hydrophobic pore property in GDL because of the hydrophobicity difference between the two materials. In this model, both the hydrophilic pores and the hydrophobic pores are taken into consideration. For hydrophilic pores, capillary condensation of liquid water will occur before saturation. For example, water will condense at $0.8\,P_{sat}(T)$ in 10 nm diameter pores [20]. For hydrophobic pores, on the contrary, condensation will occur in some extent of oversaturation. The overpressure of water condensation in pores could be expressed:

$$\Delta p = k\frac{2\delta\cos\theta}{r} \tag{1}$$

Inside the fuel cell, even though the gas is not saturated, water will condense in hydrophilic micropores because of the negative overpressure. With the increase of water vapor pressure, water will condense in smaller pores first and then bigger ones. When the gas is fully saturated, all the hydrophilic pores are flooded with liquid water. With further increase of water vapor pressure, water will condense in hydrophobic pores when water vapor pressure exceeds condensation threshold pressure in hydrophobic pores with some diameter. As the overpressure value is positive and greater for smaller pores, water will first condense in bigger pores and then smaller pores with the increase of oversaturation. So corresponding to different saturation condition along the flow channel in fuel cell, there will be different threshold condensation pore diameter, which will result in different local unflooded pore fraction and different local active area for electrochemical reaction. If we assume that water will not condense in the flow channel and water vapor in the flow channel is in equilibrium with the liquid water in GDL, there will be water form and transport balance. Along the channel, the GDL is partially flooded to different extent; however, the fuel cell could be in steady operation without apparent flooding phenomenon being observed. The partial flooding process is illustrated in Fig. 1.

3. Model development and experimental

3.1. Model assumptions

In this model, some assumptions are applied:

1. The GDL is composed of a series of pores with different diameters. There are hydrophilic pores and hydrophobic pores; at every local position, the hydrophilic pores and the

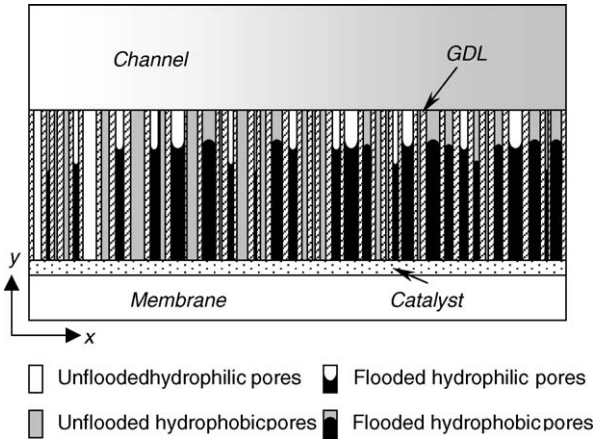

Fig. 1. Illustration of a fuel cell with partial flooded GDLs.

hydrophobic pores have the same property of pore diameter distribution.
2. Water cannot condense in flow channels.
3. Oxygen and hydrogen will not dissolve in water.
4. Catalyst layer is assumed to be an ultra-thin layer.
5. Reactants in flow channel is assumed to be plug flow.

In the first assumption, the same pore size distribution information is assumed for hydrophilic and hydrophobic pores at any location of the GDL. The pores are assumed to be in the same length. The second assumption excludes the behavior of water draining with droplets, which is difficult to express in mathematical model. We assume that water can only condense in the GDL pores, not in the flow channel, and that water is drained out of the fuel cell in gaseous state in oversaturation. Hydrogen and oxygen are assumed to be indissolvable in water, so the gases could not transport to the catalyst layer through the flooded pores. In this model, as the main concern is the flooding of GDL, gas species concentration in the flow channel is not so important, so plug flow is assumed.

3.2. Model equations

3.2.1. Species in flow channels

As the flow type being simplified to be plug flow [3], when the fuel cell is working with current density j, the gas species conservation equation along the flow channel could be expressed:

$$\frac{\mathrm{d}M_i}{\mathrm{d}x} = \xi_i \frac{\mathrm{w}j}{4F}, \quad \begin{cases} \xi_\mathrm{h} = -2; \xi_\mathrm{w,a} = -4\alpha; & \text{anode channel} \\ \xi_\mathrm{o} = -1; \xi_\mathrm{w,c} = 2 + 4\alpha; \xi_\mathrm{n} = 0; & \text{cathode channel} \end{cases} \tag{2}$$

Here anode and cathode reactants are considered to be in co-flow pattern. The net water drag coefficient α means that there will be α mole H_2O transport from anode to cathode together with 1.0 mole H^+ apparently.

Molar fraction of species in flow channels are:

$$X_i = \frac{M_i}{\sum M} \tag{3}$$

3.2.2. Mass transport in GDL

According to Maxwell–Stefan equation, molar fraction gradient of hydrogen in the anode GDL could be expressed:

$$\frac{\mathrm{d}X_\mathrm{h}}{\mathrm{d}y} = \frac{1}{\mathrm{c}D_\mathrm{hw}}(X_\mathrm{h}N_\mathrm{w,a} - X_\mathrm{w,a}N_\mathrm{h}) \tag{4}$$

where the flux of hydrogen and water are related to the local current density j and net water drag coefficient α:

$$N_\mathrm{w,a} = -\alpha\frac{j}{F}, \quad N_\mathrm{h} = \frac{j}{2F} \tag{5}$$

So Eq. (4) changes to be:

$$\frac{\mathrm{d}X_\mathrm{h}}{\mathrm{d}y} = \frac{1}{\mathrm{c}D_\mathrm{hw}}\frac{j}{2F}[(2\alpha+1)X_\mathrm{h} - 1] \tag{6}$$

For a specific position along the flow channel, if local current density is fixed, α will be fixed and Eq. (6) could be integrated directly to be:

$$X_\mathrm{h} = \left(X_\mathrm{h}^\mathrm{channel} - \frac{1}{2\alpha+1}\right)\exp\left[\frac{j}{2F}\frac{y(2\alpha+1)}{\mathrm{c}D_\mathrm{hw}}\right] + \frac{1}{2\alpha+1}; \quad X_\mathrm{w,a} = 1 - X_\mathrm{h} \tag{7}$$

For cathode GDL, molar fraction gradients for the species are:

$$\frac{\mathrm{d}X_i}{\mathrm{d}y} = \sum_j \left(\frac{X_iN_j - X_jN_i}{\mathrm{c}D_{ij}}\right),$$

$$\begin{pmatrix} N_\mathrm{o} \\ N_\mathrm{n} \\ N_\mathrm{w,c} \end{pmatrix} = \frac{j}{4f}\begin{pmatrix} 1 \\ 0 \\ -2-4\alpha \end{pmatrix} \tag{8}$$

This equation could be rewritten as:

$$\frac{\mathrm{d}}{\mathrm{d}y}\begin{pmatrix} N_\mathrm{o} \\ N_\mathrm{n} \\ N_\mathrm{w,c} \end{pmatrix} = \frac{j}{4F}\begin{pmatrix} -\dfrac{X_\mathrm{n}}{\mathrm{c}D_\mathrm{on}} - \dfrac{(4\alpha+2)X_\mathrm{o}}{\mathrm{c}D_\mathrm{ow}} - \dfrac{X_\mathrm{w,c}}{\mathrm{c}D_\mathrm{ow}} \\ \dfrac{X_\mathrm{n}}{\mathrm{c}D_\mathrm{on}} - \dfrac{(4\alpha+2)X_\mathrm{n}}{\mathrm{c}D_\mathrm{nw}} \\ \dfrac{(4\alpha+2)X_\mathrm{o}}{\mathrm{c}D_\mathrm{ow}} + \dfrac{X_\mathrm{w,c}}{\mathrm{c}D_\mathrm{ow}} + \dfrac{(4\alpha+2)X_\mathrm{n}}{\mathrm{c}D_\mathrm{nw}} \end{pmatrix} \tag{9}$$

The binary diffusion coefficients in the former equations are related with temperature and can be found in [21]:

$$\begin{aligned} \mathrm{c}D_\mathrm{hw} &= 3.68\times10^{-5}(T/307)^{1.10} \quad \mathrm{mol\,cm^{-1}\,s^{-1}} \\ \mathrm{c}D_\mathrm{on} &= 8.40\times10^{-6}(T/293)^{1.06} \quad \mathrm{mol\,cm^{-1}\,s^{-1}} \\ \mathrm{c}D_\mathrm{nw} &= 1.01\times10^{-5}(T/293)^{1.07} \quad \mathrm{mol\,cm^{-1}\,s^{-1}} \\ \mathrm{c}D_\mathrm{ow} &= 1.01\times10^{-5}(T/293)^{1.08} \quad \mathrm{mol\,cm^{-1}\,s^{-1}} \end{aligned} \tag{10}$$

The binary diffusion coefficients are modified to effective diffusivity with Bruggeman relation as used in many models [2,3]:

$$D_{ij}^\mathrm{eff} = D_{ij}\varepsilon^{1.5} \tag{11}$$

Saturated water vapor pressure at temperature T could be expressed in [3]:

$$\log P_{\text{sat}} = -19.0437 + 0.1084T - 2.1022 \times 10^{-4}T^2 + 1.4454 \times 10^{-7}T^3 \quad (12)$$

Once the molar fractions of the species are known, we know the saturation extent inside GDL and the threshold flooding pore radius according to Eq. (1) for anode and cathode GDL.

$$r_{\text{a}} = k\frac{2\delta\cos\theta}{pX_{\text{w,a}}^{\text{catalyst}} - P_{\text{sat}}}, \qquad r_{\text{c}} = k\frac{2\delta\cos\theta}{pX_{\text{w,c}}^{\text{catalyst}} - P_{\text{sat}}} \quad (13)$$

As discussed in Section 2, hydrophilic pores with radius smaller than this threshold radius or hydrophobic pores with radius larger than the threshold radius are not flooded with liquid water and available for gas transportation, and the corresponding catalyst area is available for electrochemical reactions, so if the pore radius distribution of the GDL is known, the unflooded pore area fraction, also active catalyst surface area fraction, could be calculated with the threshold radius:

$$f_{\text{a}}^{\text{philic}} = \frac{\int_{r_{\text{a}}}^{\infty}\psi_{\text{a}}(r)\,\text{d}r}{\int_{0}^{\infty}\psi_{\text{a}}(r)\,\text{d}r}, \quad f_{\text{a}}^{\text{phobic}} = \frac{\int_{0}^{r_{\text{a}}}\psi_{\text{a}}(r)\,\text{d}r}{\int_{0}^{\infty}\psi_{\text{a}}(r)\,\text{d}r},$$
$$f_{\text{c}}^{\text{philic}} = \frac{\int_{r_{\text{c}}}^{\infty}\psi_{\text{c}}(r)\,\text{d}r}{\int_{0}^{\infty}\psi_{\text{c}}(r)\,\text{d}r}, \quad f_{\text{c}}^{\text{phobic}} = \frac{\int_{0}^{r_{\text{c}}}\psi_{\text{c}}(r)\,\text{d}r}{\int_{0}^{\infty}\psi_{\text{c}}(r)\,\text{d}r} \quad (14)$$

$$f_{\text{a}} = f_{\text{a}}^{\text{philic}}\chi + f_{\text{a}}^{\text{phobic}}(1-\chi),$$
$$f_{\text{c}} = f_{\text{c}}^{\text{philic}}\chi + f_{\text{c}}^{\text{phobic}}(1-\chi) \quad (15)$$

f^{philic} and f^{phobic} are unflooded pore fraction of hydrophilic pores and hydrophobic pores. The integrations of the pore size distribution function ψ results in pore volume, because the pores are assumed to be in the same length, the volume ratio is also unflooded pore area fraction. The unflooded pore area fraction is the sum of hydrophilic pore fraction and hydrophobic pore fraction.

Pore size distribution of GDL was shown to have micropores and macropores [19,22] with back layer on carbon cloth GDL, and macropores (5–20 μm) same to perform flooding-proof function [19]. Pore size distribution in Toray carbon paper was measured and shown to have dominant macropores in 5–100 μm range without active carbon back layer, and the average pore diameter was measured to be 23, 19 and 17 μm for 0, 16 and 35% PTFE content in carbon paper [23]. In our previous study, pore size distribution of Toray carbon paper (TGP-H-060) with active carbon back layer was measured and results showed that most of the pores are in 0–20 μm diameter range, and the average pore diameters are 10, 7 and 5 μm for 24, 35 and 42% PTFE in carbon paper, respectively [24,25]. The GDL pore size distribution is close to normal distribution. In this model, we use normal distribution function to fit the experimental pore size distribution with 24% PTFE in carbon paper, average pore diameter of which is 10 μm. The pore size distribution function is:

$$\psi_{\text{a}}(r) = \psi_{\text{c}}(r) = \frac{1}{\sqrt{2\pi}\omega}\text{e}^{-1/2\omega^2(r-r_0)^2} \quad (16)$$

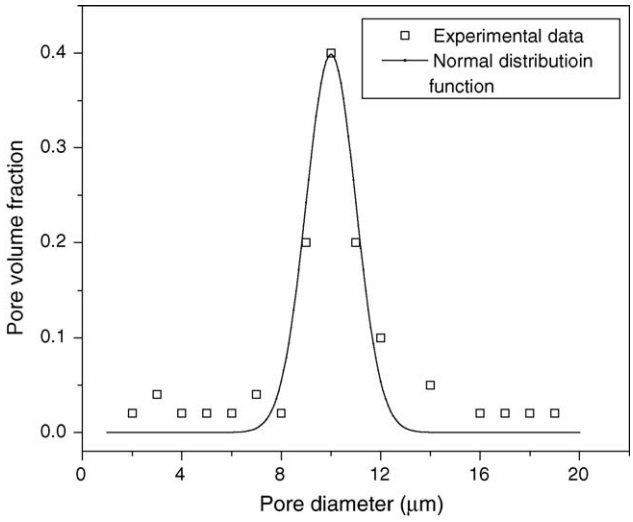

Fig. 2. Experimental GDL pore size distribution from reference [24] and normal distribution function.

Fig. 2 shows the experimental distribution result and the fit curve, where $r_0 = 10$ μm and $\omega = 1$. With Eqs. (14)–(16), for a specified pore radius, r, the unflooded pore area fraction f_{a} and f_{c} could be calculated.

3.2.3. Water transport through membrane

There are three mechanisms for water transport through membrane [26]: electro-osmotic drag with proton transport, back diffusion by water concentration gradient and convection by pressure difference. In this model, water convection is not taken into account because balanced pressures are applied. So water transport equation in membrane could be written as [3]:

$$n_{\text{d}}\frac{j}{F} - \frac{\rho_{\text{m}}}{M_{\text{m}}}D_{\text{w}}\frac{\text{d}\lambda}{\text{d}y} = \alpha\frac{j}{F} \quad (17)$$

In Eq. (16) the electro-osmotic drag coefficient and diffusion coefficient are from [3,27], respectively:

$$n_{\text{d}} = \frac{2.5}{22}\lambda \quad (18)$$

$$D_{\text{w}} = 2.1 \times 10^{-3}\lambda\,\exp\left(-\frac{2436}{T}\right) \quad (19)$$

At the interface of membrane and catalyst, activity of water in membrane phase is equal to that in gaseous phase, which is related to the partial pressure of water in gas:

$$a_{\text{w}} = X_{\text{w}}\frac{p}{P_{\text{sat}}} \quad (20)$$

Water content in membrane, λ, which is defined as the ratio between the number of water molecules to the number of charge sites ($SO_3^-H^+$), is related to water activity in membrane according to the relation given in [3]:

$$\lambda = \begin{cases} 0.043 + 17.81a_{\text{w}} - 39.85a_{\text{w}}^2 + 36.0a_{\text{w}}^3 & 0 < a_{\text{w}} \le 1 \\ 14.0 + 1.4(a_{\text{w}} - 1) & 1 < a_{\text{w}} \le 3 \end{cases} \quad (21)$$

3.2.4. Electrochemistry

Butler–Volmer equations are utilized to calculate current density as listed in Eq. (22). Only the unflooded catalyst surface will contribute to the electrochemical reaction, therefore, the function of the catalyst active area fraction appears in these equations.

$$j_a = f_a j_a^0 \left(\frac{X_h^{cat}}{X_h^{ref}}\right)^{0.5} \left[\exp\left(\frac{\alpha_a F}{RT}\eta_a\right) - \exp\left(-\frac{(1-\alpha_a)F}{RT}\eta_a\right)\right]$$
$$j_c = f_c j_c^0 \frac{X_o^{cat}}{X_o^{ref}} \left[\exp\left(\frac{\alpha_c F}{RT}\eta_c\right) - \exp\left(-\frac{(1-\alpha_c)F}{RT}\eta_c\right)\right] \quad (22)$$

Cathode exchange current density is considered to vary with temperature with a relation from literature [28], where the activation energy ΔE has a value of 27.7 kJ mol^{-1}.

$$j_{c,2}^0 = j_{c,1}^0 \exp\left[-\frac{\Delta E}{R} \times \left(\frac{1}{T_2} - \frac{1}{T_1}\right)\right] \quad (23)$$

Cathode transfer coefficient also varies with temperature according to the following relationship [28]:

$$\alpha_c = 0.495 + 2.3 \times 10^{-3}(T - 300) \quad (24)$$

To determine the ohmic drop of the membrane, empirical relation from [3] is used to calculate the conductivity:

$$\sigma_m = (5.139\lambda - 3.26) \times 10^{-3} \exp\left[1268 \times \left(\frac{1}{303} - \frac{1}{T}\right)\right] \quad (25)$$

So the membrane resistance could be calculated by integration over the membrane thickness:

$$R_m = \int_0^{d_m} \frac{1}{\sigma_m} dy \quad (26)$$

With the overpotentials known, the cell voltage is easy to know by subtraction the overpotentials from the open circuit voltage:

$$V_{cell} = V_{oc} - \eta_a - \eta_c - jR_m \quad (27)$$

The thermodynamic open circuit voltage V_{oc} is a function of temperature and reactants partial pressure with Nernst equation shown below [28]:

$$V_{oc} = 1.229 - 8.456 \times 10^{-4}(T - 298.15) + 4.31 \times 10^{-5} T \ln(p_{H_2} p_{O_2}^{0.5}) \quad (28)$$

With the current density distribution j known, average current density of the fuel cell at a specified voltage value could be calculated by integrating j along the whole length of the flow channel:

$$i = \frac{1}{L}\int_0^L j(x)\, dx \quad (29)$$

3.3. Solution method

The calculation domain is discretized in x and y direction and the equations are solved numerically at a specified cell voltage. At a discretized fraction along the flow channel, current density j and net water drag coefficient α are first guessed, and molar fraction of the species in anode GDL could then be calculated algebraically in Eq. (7) and numerically with fourth-order Runge-Kutta method for cathode GDL in Eq. (9). Threshold pore radii for anode and cathode r_a and r_c could then be calculated and then the unflooded pore fractions f_a and f_c. Water content in membrane λ is calculated by integrating Eq. (17) in y direction numerically with fourth-order Runge-Kutta method and gain a new net water drag coefficient α. If the difference between new α and the old one is greater than a specified error 10^{-3}, an iteration loop will be performed with secant method. With a proper α found, overpotentials and cell voltage are calculated. If the cell voltage difference between specified value and calculated value is higher than error, another iteration loop is used to search for a correct current density j with secant method. This process is performed for each discretized fraction from the inlet to the outlet, and then the average current density could be calculated by integrating the current density distribution along the flow channel.

3.4. Experimental

Carbon paper (Toray TGP-H-060) was immersed in 30% PTFE latex (Dupont) for 10 min and dried in air and then heat-treated at 350 °C for 1 h, after sprayed active carbon (VulcanXC-72, Cabot Corp.) for back layer, heat-treated again. Pt/C electrocatalyst (Johnson–Matthey) was dispersed in ethanol solution and sprayed to the surface of the back layer, with Pt loading 0.4 mg cm^{-2}. Then the GDL was treated in vacuum dryer at 140 °C for 1 h. The treated GDL was then cut in 5 cm^2 foursquare pieces. Pretreated Nafion 112 membrane (Dupont) with 5 vol.% H_2O_2 (Beijing Chemical) solution and 0.5 M H_2SO_4 solution was sandwiched with two pieces of GDL and hot-pressed at 5 MPa to form a membrane electrode assembly (MEA). Fuel cell performance was measured with Arbin fuel cell test stand. Hydrogen and air are humidified with membrane humidifier from Beijing LN Power Sources Co. Ltd.

The former mentioned pore size distribution measurement in [24,25] was conducted with 9500 Mercury Porosimetry (Micromeritics Instrument Corp., USA). The sample was the carbon paper with active carbon back layer prepared in the procedure mentioned above.

4. Results and discussion

4.1. Base case

Parameters used in this model are listed in Table 1. Operation conditions of the base case are listed in Table 2. The experimental fuel cell is a 5 cm^2 single cell with co-flow serpentine channels. The width of the channel and the rib is 1 mm, and channel length is 25 cm. In the model, the channel width is set to be 2 mm, which is the sum of channel width rib width. It needs be pointed out that, in the along the channel model, the information in the cross channel direction could not be presented; there is some difference between the 2D model and 3D model, which will be further discussed in the following sections. As the active area is

Table 1
Parameters used in the model

Parameters	Symbol	Value	Unit
Channel width	w	0.2	cm
Channel length	L	25	cm
GDL thickness	d_{GDL}	200	μm
Membrane thickness	d_m	50	μm
Membrane equivalent weight	M_m	1100	g mol^{-1}
Dry membrane density	ρ	1.0	g cm^{-3}
Water surface tension	δ	7.28×10^{-6}	J cm^{-2}
Anode transfer coefficient	α_a	0.5	–
Cathode transfer coefficient	α_c	0.5	–
Anode exchange current density	j_a^0	1.0	A cm^{-2}
Cathode exchange current density (343 K)	j_c^0	0.002	A cm^{-2}

Table 2
Operation conditions for the base case

Parameters	Value	Unit
Temperature of fuel cell	70	°C
Relative humidity of reactants	90	%
Pressure of reactants	0.2	MPa
Flux of H_2	0.10	SL min^{-1}
Flux of air	0.20	SL min^{-1}
Average pore diameter of GDL	10	μm
Porosity of GDL	60	%
Hydrophilic pore volume fraction	30	%
Contact angle of hydrophilic pores	75	°
Contact angle of hydrophobic pores	125	°

the same in the model and in experimental cell, the same base case conditions are applied for both the experimental and model.

Fig. 3 shows the current density distribution along the flow channel in base case at different discharge voltages: 0.7, 0.6, 0.5 and 0.4 V. It is shown that the current density is relatively uniform distributed at high cell voltage, e.g. 0.7 V, decrease slowly along the channel. With the decrease of cell voltage, current density increases quite much in the inlet region, and decreases

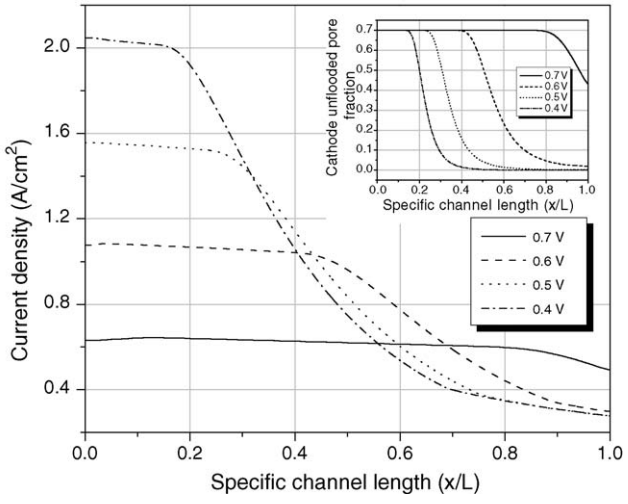

Fig. 3. Current density and cathode unflooded pore fraction (subplot) along the flow channel at different discharge voltage in base case. Operation conditions are listed in Table 2.

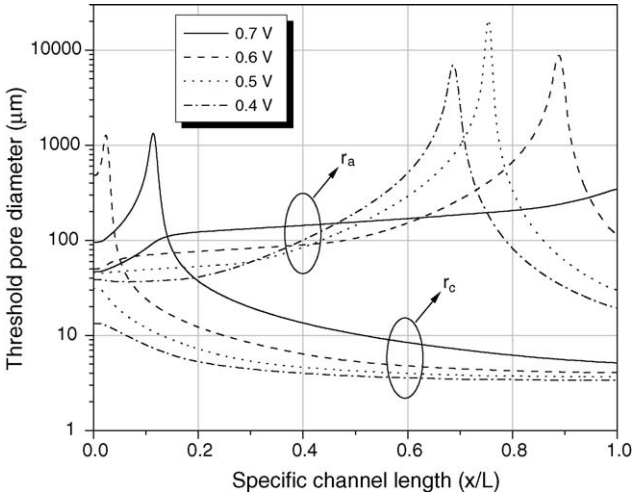

Fig. 4. Threshold pore diameter along the flow channel at different discharge voltage in base case.

along the channel. Greater current density gradient is shown for lower voltage. This current density distribution behavior is similar to the experimental results in our previous report [29] and other literature [30]. In Fig. 3, the subplot is the cathode unflooded pore fraction at different cell voltage. It shows that the cathode unflooded pore fraction is smaller than 0.7, means that all hydrophilic pores are flooded (hydrophilic pores takes 30% of the pore volume as listed in Table 2). Along the channel, with the increase of water activity (see Fig. 5), smaller and smaller hydrophobic pores will be flooded (see Fig. 4), results in lower and lower unflooded cathode GDL pore fraction and active reaction area, so current density decrease along the channel. At lower cell voltage, more water is produced and the unflooded pore fraction begins to drop at a nearer place to the inlet.

Fig. 4 shows the threshold pore diameter for both anode and cathode. With the normal distribution shown in Fig. 2, it is clear that the pore volume fraction is almost zero when pore diameter is greater than 16 μm, however, for the calculation, a wide range of pore diameter is taken in consideration even though the pore volume is very small. The picks in the curves in Fig. 4 reveal at where the gas is just in saturation, and where the hydrophilic pores are totally flooded. Before the picks, the threshold diameters are for hydrophilic pores, and the values after the picks are for hydrophobic. In this figure, the cathode threshold diameters fall into the macropore range, which influence the current density greatly.

Fig. 5 shows the species distribution inside the GDLs and membrane. It shows that even the feed air is not saturated, in the GDL, the gas is oversaturated from the inlet; results in water activity in cathode GDL higher than 1.0 and membrane water content higher than 14 on the cathode side. Oxygen concentration gradient in the inlet region is higher than the outlet region, corresponding to higher current density in the inlet region. On the anode side, with the consumption of hydrogen, water activity increases gradually from the inlet to the outlet. Near the outlet, hydrogen is in oversaturation.

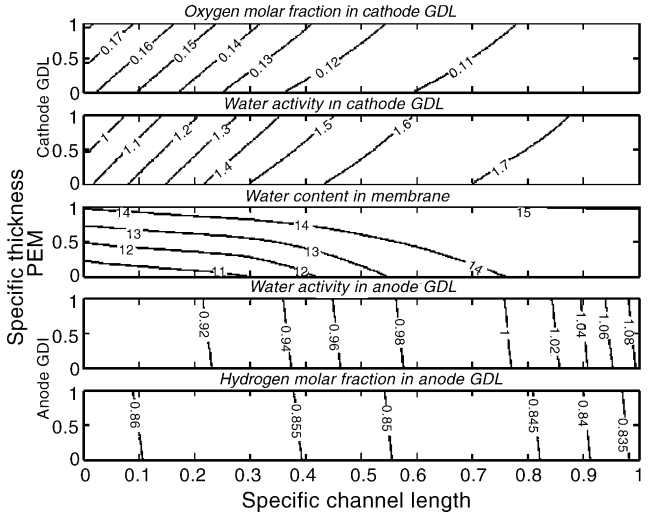

Fig. 5. Species distribution in GDLs and membrane at 0.5 V discharge in base case.

4.2. Cell temperature

Operation temperature impacts fuel cell performance obviously. A higher temperature will not only activate the reactions on the catalyst surface, but also accelerate the species transportation. Performances of the fuel cell at four temperatures 40, 50, 60 and 70 °C are measured experimentally and calculated with the model. Polarization curves are shown in Fig. 6, where plot (a) is the experimental results and (b) is the model results. Reactants are humidified at the same temperature to the fuel cell reaction. In the model, relative humidity of the reactants is fixed to be 90%. It illustrated that the experimental and calculated polarization curves are very similar. A better performance is shown at higher temperature: higher cell voltage at a specified current density value, higher limiting current density, and lower slope of the curve in moderate voltage range which indicates lower resistance, which could be seen from membrane ohmic resistivity and overpotential shown in Fig. 7. Relationship between membrane resistivity and cell temperature is clearly shown in Eq. (25). In Fig. 6(b), the cathode activation overpotential is also shown. The cathode overpotential difference between two temperatures is shown to be higher than the cell voltage difference, this is because at higher temperature, thermodynamic V_{oc} is lower from Eq. (28). V_{oc} will decrease about 10 mV when temperature increases 10 K.

4.3. Reactants humidity

Because the conductivity of perfluorinated proton conducting membrane relies greatly on the water content, reactants need to be humidified to enhance performance of fuel cell. In Fig. 8, experimental results and model results of the fuel cell with humidification temperature 50, 60 and 70 °C are shown. We assume that the relative humidity of reactants out of the humidifier is 90% to the humidification temperature. Fuel cell temperature is fixed to be 70 °C. Use Eq. (12), we can calculate that the reactants with 60 °C humidification is 76.8% RH

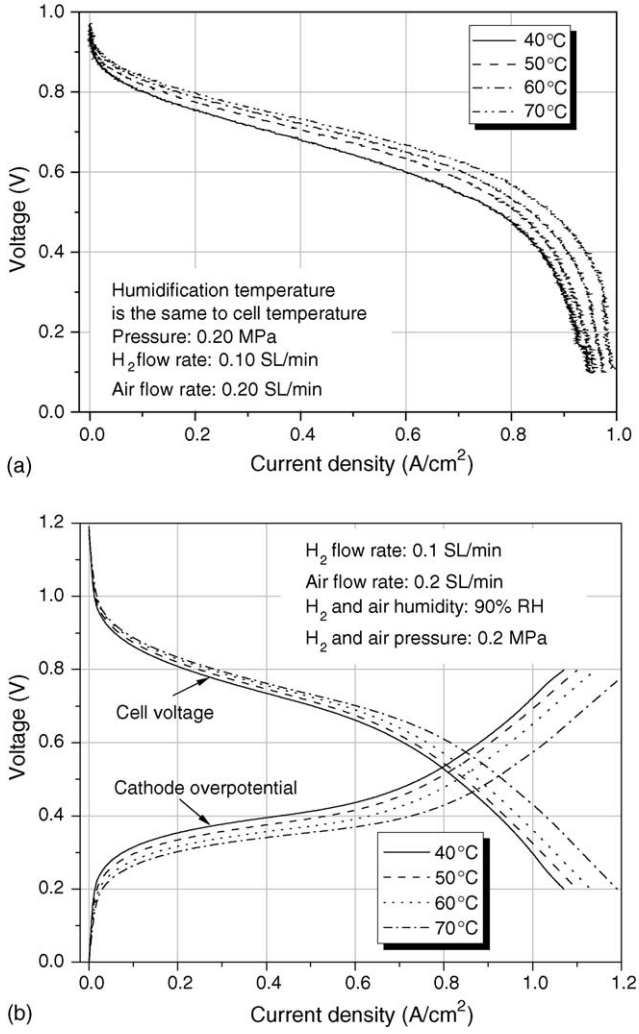

Fig. 6. Polarization curves of the fuel cell at different temperature (a) experimental results; (b) model results.

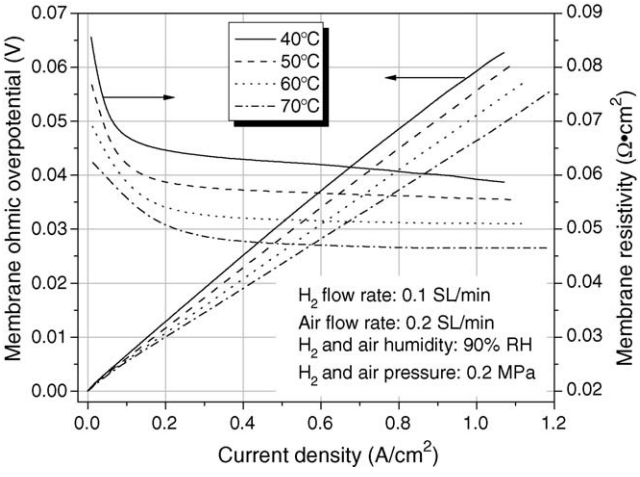

Fig. 7. Membrane resistivity and ohmic overpotentials at different operation temperatures.

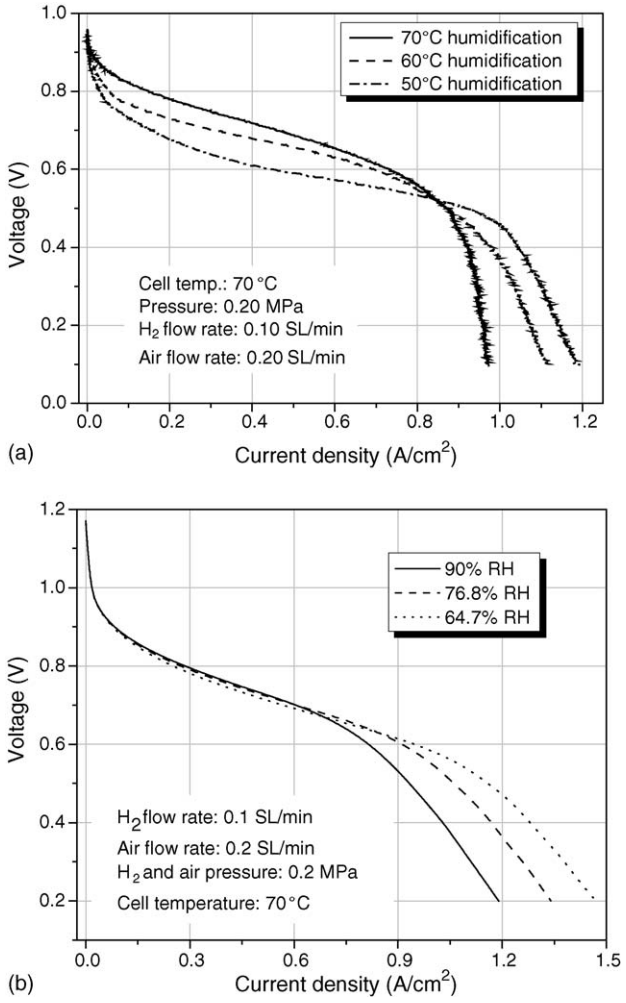

Fig. 8. Polarization curves of the fuel cell with different reactants relative humidity (a) experimental results; (b) model results.

and 50 °C humidification to be 57.6% RH for 70 °C reaction. In Fig. 8(a), the experimental polarization curves show that, with lower humidification temperature, the fuel cell behaves worse performance in high voltage range 0.5–1 V, but has higher limiting current density. Similar behavior is shown in the model results in Fig. 8(b) give. Nevertheless, the model is not sensitive enough to reveal experimental details. For the experimental curves, there are great differences in high voltage range (>0.8 V), which is not shown in the model curves. This indicates that the catalyst activity is greatly reduced with lower temperature humidification, which might be attributed to active catalyst surface loss: with low humidity, the proton conductive ionomer agglomerates in the catalyst layer will dehydrate and at least partially loss their conductivity, which will make the platinum catalyst particles attached on them insufficiently utilized; as a result, effective catalyst surface is reduced and greater activation overpotential is shown. Unfortunately, this effect is not taken into account in the present model as the catalyst layer is simplified to be an ultra-thin layer.

Fig. 9 shows current density and membrane resistivity distribution along the flow channel at 0.5 V discharge with different reactants humidity. With lower humidity, the membrane resistivity is much greater at the inlet region. With water produced along the channel, membrane resistivity decreases and the current density increases. When the gases are in oversaturation, parital flooding will make the current density drop again. As a result, the current density distribution for 64.7% RH and 76.8% RH forms a "hill" like shape. Fig. 10 shows the current density distribution with 64.7% RH reactions feed at different discharge voltage. It illustrated that, at 0.7 V discharge, different to the current density distribution at base case, current density increases along the flow channel. With the decrease of cell voltage, current density increase rate in the middle of the channel is higher than the inlet region, and current density in the outlet region begins to drop because of flooding. As a result, the membrane without fully saturation and GDL flooding effect are shown. This current density distribution trend is similar to the experimental results in our former report [29]. Although the operation conditions here are different to those in [29], and it is not logical to say the model current density distribution is "validated" by experimental, the distribution trend is similar to some extent. It seems that the dehydration effect is underestimated and flooding

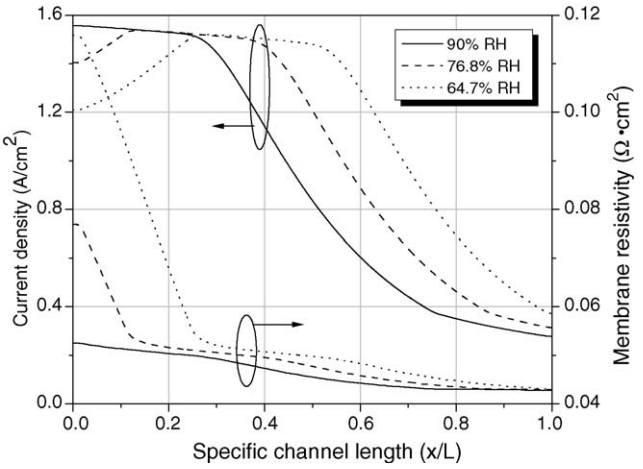

Fig. 9. Current density and membrane resistivity distribution along the flow channel at different humidification temperature at 0.5 V discharge.

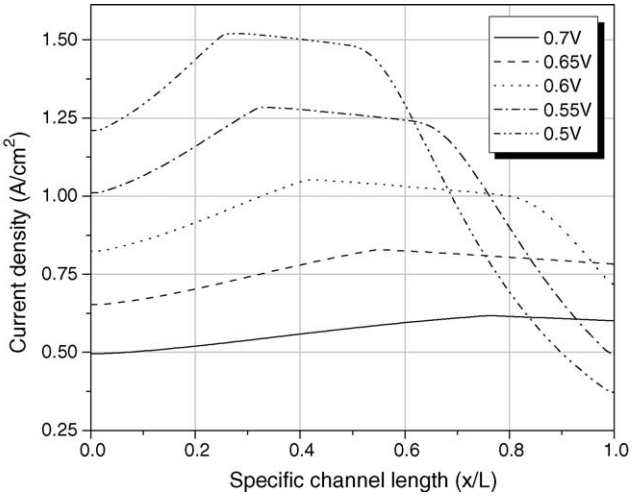

Fig. 10. Current density distribution along the flow channel at different discharge voltage with 64.7% RH reactants feed.

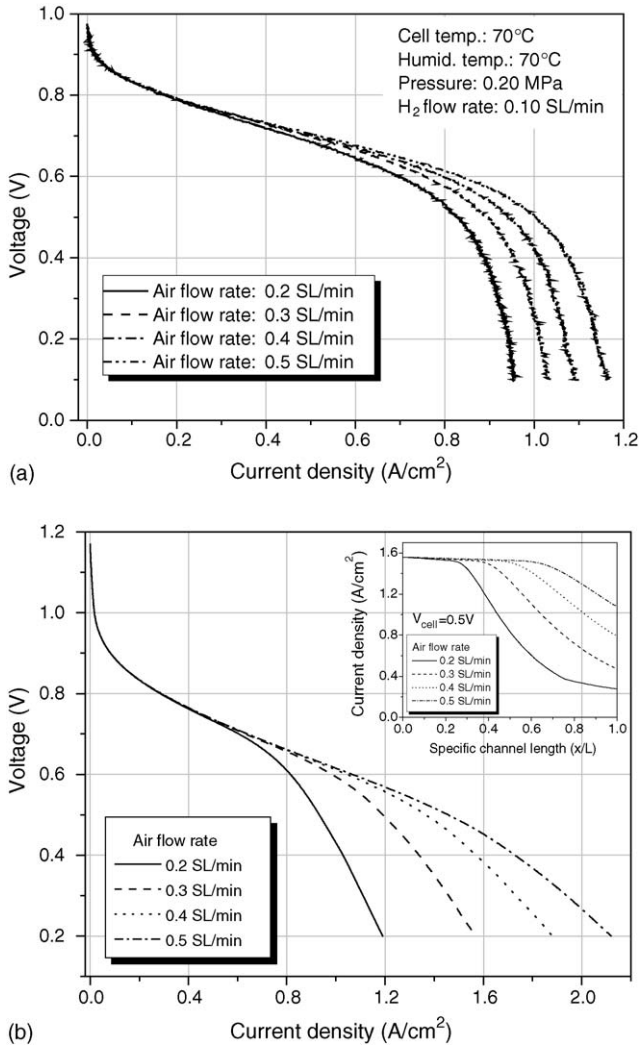

Fig. 11. Polarization curves of the fuel cell with different air flow rates (a) experimental results; (b) model results.

effect is overestimated compared with the experimental results. We believe that the this model will be more delicate to predict the current density distribution if it more details inside GDL and catalyst were taken into account.

4.4. Reactants flow rate

4.4.1. Vary air flow rate

If a fuel cell is operating with higher air flow rate, air stoichiometry in another word, not only oxygen gradient along flow channel and through GDL will be reduced, but also flooding will be lightened, as a result, a better fuel cell performance is achieved. However, fuel cell efficiency will decrease because more energy is needed for the air compressor or air fan. The influence of air flow rate to fuel cell performance is shown in Fig. 11(a) and (b) in experimental and in model, respectively. A higher limiting current density is exhibited with greater air flow rate. Experimental results show limiting current density increases from 0.9 to 1.19 A cm^{-2} when air flux increases from 0.2 to 0.5 SL min^{-1}. However, the model results show greater

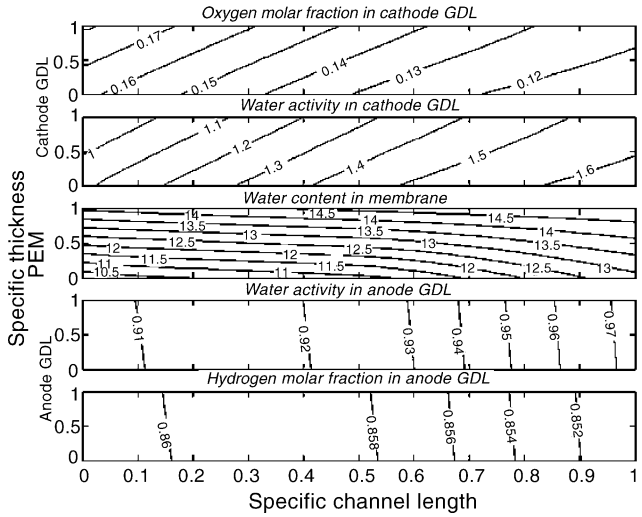

Fig. 12. Species distribution in GDLs and membrane at 0.5 V with 0.4 SL min^{-1} air flow rate.

current density increase. One of the reasons for this might be the ignorance of the current density difference in the cross channel direction in 2D model. As shown in [28], current density shows much difference between the place beneath the channel and beneath the rib, especially at high overpotential operation. The omission of the collector will overestimate mass transfer and chemical reaction rate beneath the rib at high current density operation. The difference between 2D model and 3D model was also clearly shown in [31], where much current density difference is shown at low cell voltage.

As shown in the subplot of Fig. 11, where current density for different air flow rate at 0.5 V discharge is shown, with higher air flow rate, cathode flooding is lighter and current density in the outlet region is higher. Fig. 12 shows the species distribution in GDLs and membrane for 0.4 SL min^{-1} air flow rate at 0.5 V discharge. Compared with the base case in Fig. 5, it is clear that with higher air flow rate, higher oxygen and water gradient is shown in GDL and membrane in y direction, and smaller water activity in cathode GDL will result in lighter flooding. Thus, higher air flow rate will be helpful for water removal and flooding prevention.

4.4.2. Vary hydrogen flow rate

For the case of different hydrogen flow rate, the experimental results (Fig. 13(a)) show almost overlapped polarization curves. Different to oxygen in cathode gas, in which the reacting agent, oxygen, is less than 20% because the dilution of nitrogen, hydrogen in the anode gas is higher than 80%. Stoichiometry does not have great impact on the concentration of hydrogen. More importantly, hydrogen oxidation reaction is very rapid compared with oxygen reduction. Furthermore, hydrogen diffusivity is higher than oxygen. These are the reasons for very little impact shown for different hydrogen flow rate. The model results (Fig. 13(b)) also show very small difference in the polarization curves. The species distribution plot (not shown) with 0.2 SL min^{-1} H_2 flow rate at 0.5 V shows very little difference to the base case in Fig. 5.

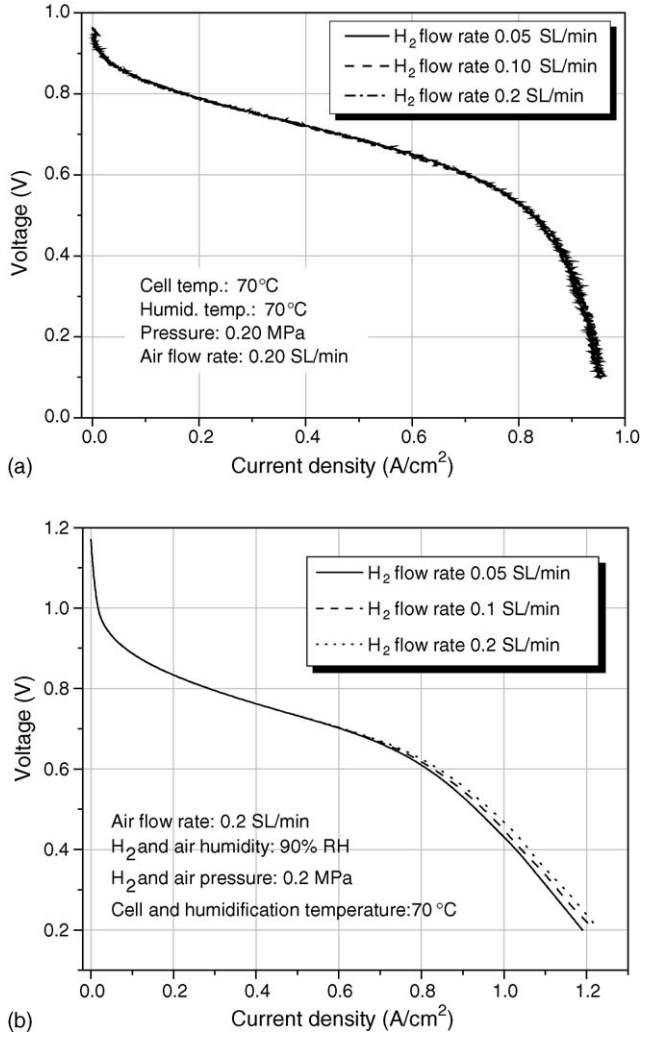

Fig. 13. Polarization curves of the fuel cell with different hydrogen flow rates (a) experimental results; (b) model results.

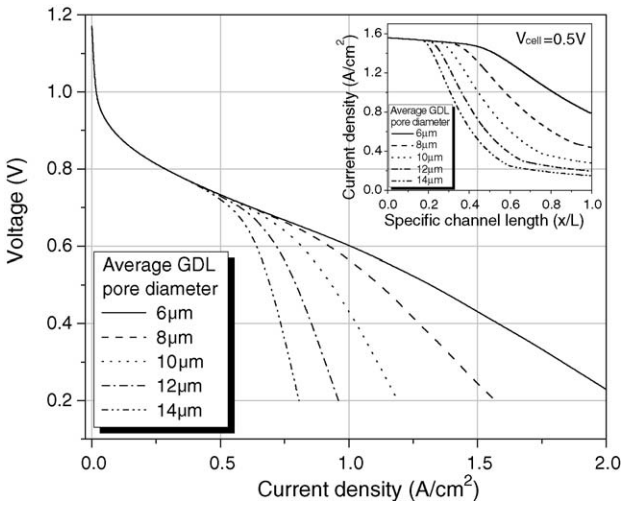

Fig. 14. Influence of GDL average pore diameter on fuel cell performance.

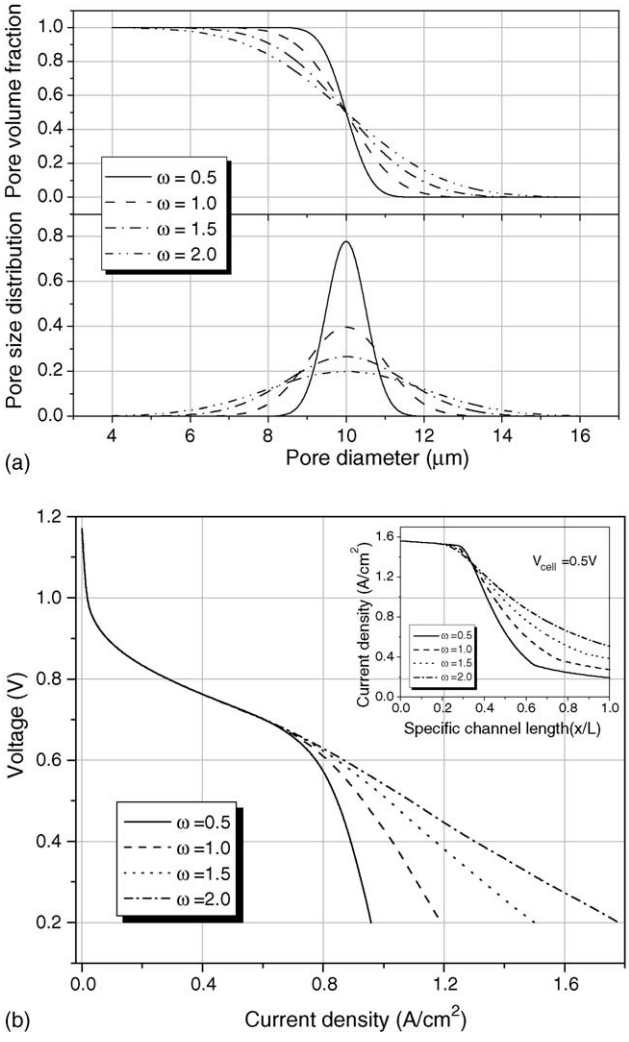

Fig. 15. Influence of GDL pore distribution on the fuel cell performance (a) pore size distribution with different normal distribution function coefficients; (b) polarization curves.

4.5. GDL property

4.5.1. Average pore diameter

Fig. 14 shows the influence of GDL average pore diameter on fuel cell performance, and the subplot is current density at 0.5 V discharge. In Eq. (1), it is clear that a smaller average pore diameter will result in higher overpressure for water condensation in the hydrophobic pores. Fig. 14 shows performance of five average pore diameter values: 6, 8, 10, 12 and 14 μm. Difference is shown in low voltage range: for a smaller GDL average pore diameter, overpressure for the hydrophobic pores will be higher, and that the flooding is lighter, so higher current density is shown.

4.5.2. Pore size distribution

As normal distribution function is utilized in the model to simulate GDL pore distribution, the coefficient ω in the function is modified to study the influence of pore size distribution to cell performance. Fig. 15 shows the pore size distribution with different ω values and the accumulated volume fractions integrated from macro pores to micro pores. With a greater ω

value, the GDL pores distribute in a broader diameter range. The polarization curves in Fig. 15(b) show difference in concentration polarization range: with a greater ω value, the cell voltage drops flatter. The trend is also shown in the current density distribution curves in 0.5 V discharge in the subplot. Current density begins to drop at a nearer place from the inlet end for a greater ω value, but higher to the outlet end. A broader pore size distribution is favorable for more uniform current density distribution.

It must be acknowledged that the "validation" of the model was limited in comparing a set of fuel cell polarization curves with experimental results, which might not be rigorous enough, because the actual physical processes are much more complicate than the present understanding and the polarization curve is only a gross behavior of all the microcosmic processes. Although the current density distribution trend is similar to experimental results to some extend, the detailed behavior predicted by the model has not been validated by experiments, and as such, the predictions do not necessarily represent the actual behavior of an operating fuel cell.

5. Conclusions

A two dimensional partial flooding model, in which GDL pore size distribution is first taken into consideration, is developed to study the influence of liquid water to the performance of PEMFC. In this model, liquid water produced is considered to condense first in hydrophilic pores and then in hydrophobic pores if water vapor pressure is higher than the condensation pressure for the pores. The partial flooding will reduce the active reaction area in turn. Use this model, different operation conditions are studied and the model results show reasonable accordance with experimental results.

Acknowledgement

Financial support of "National 973 Project on Hydrogen Energy (TG2000026410)" is gratefully acknowledged.

References

[1] Z.Q. Mao, Fuel Cells, Chemical Industry Press, Beijing, 2005 (in Chinese).
[2] D.M. Bernardi, M.W. Verbrugge, J. Electrochem. Soc. 139 (9) (1992) 2477–2491.
[3] T.E. Springer, T.A. Zawodzinski, S. Gottesfeld, J. Electrochem. Soc. 138 (8) (1991) 2334–2342.
[4] T.F. Fuller, J. Newman, J. Electrochem. Soc. 145 (5) (1993) 1218–1225.
[5] A.A. Kulikovsky, J. Divisek, A.A. Kornyshev, J. Electrochem. Soc. 146 (11) (1999) 3981–3991.
[6] J.S. Yi, T.V. Nguyen, J. Electrochem. Soc. 146 (1) (1999) 38–45.
[7] S. Dutta, S. Shimpalee, J.W. Van Zee, J. Appl. Electrochem. 30 (2) (2000) 135–146.
[8] T. Berning, D.M. Lu, N. Djilali, J. Power Sources 106 (1–2) (2002) 284–292.
[9] K.Z. Yao, K. Karan, K.B. McAuley, P. Oosthuizen, B. Peppley, T. Xie, Fuel Cells 4 (1–2) (2004) 3–29.
[10] W. He, J.S. Yi, T.V. Nguyen, AIChE J. 46 (10) (2000) 2053–2064.
[11] T. Berning, N. Djilali, J. Electrochem. Soc. 150 (12) (2003) A1589–A1598.
[12] M.C. Kimble, N.E. Vanderborgh, Proc. Intersoc. Energy Convers. Eng. Conf. 27 (3) (1992) 413–417.
[13] L. You, H. Liu, Int. J. Heat Mass Transfer 45 (2002) 2277–2287.
[14] Z.H. Wang, C.Y. Wang, K.S. Chen, J. Power Sources 94 (1) (2001) 40–50.
[15] N.P. Siegel, M.W. Ellis, D.J. Nelson, M.R. von Spakovsky, J. Power Sources 128 (2004) 173–184.
[16] G. Lin, W. He, T.V. Nguyen, J. Electrochem. Soc. 151 (12) (2004) A1999–A2006.
[17] C.Y. Wang, in: W. Lietsich, A. Lamm, H.A. Gasteiger (Eds.), Handbook of Fuel Cells—Fundamentals Technology and Applications, vol. 3, John Wiley & Sons, Chichester, 2003, pp. 337–347.
[18] J.H. Nam, M. Kaviany, Int. J. Heat Mass Transfer 45 (2002) 2277–2278.
[19] C.S. Kong, D.Y. Kim, H.K. Lee, Y.G. Shul, T.H. Lee, J. Power Sources 108 (2002) 185–191.
[20] D. Bevers, M. Wöhr, K. Yasuda, K. Oguro, J. Appl. Electrochem. 27 (1997) 1254–1264.
[21] I.M. Hsing, P. Futerko, Chem. Eng. Sci. 55 (2000) 4209–4218.
[22] H.K. Lee, J.H. Park, D.Y. Kim, T.H. Lee, J. Power Sources 131 (2004) 200–206.
[23] M.F. Mathias, J. Roth, J. Fleming, W. Lehnert, in: W. Lietsich, A. Lamm, H.A. Gasteiger (Eds.), Handbook of Fuel Cells—Fundamentals Technology and Applications, vol. 3, John Wiley & Sons, Chichester, 2003, pp. 517–537.
[24] C. Wang, Z.Q. Mao, J.M. Xu, Chem. J. Chinese U. 26 (3) (2005) 531–534.
[25] C. Wang, Ph.D. thesis, Tsinghua University, Beijing, 2003.
[26] T.V. Nguyen, R.E. White, J. Electrochem. Soc. 140 (8) (1993) 2178–2186.
[27] T.F. Fuller, Ph.D. thesis, University of California, Berkeley, CA, 1992.
[28] W. Sun, B.A. Peppley, K. Karan, Electrochim. Acta 50 (2005) 3359–3374.
[29] Z.X. Liu, Z.Q. Mao, B. Wu, L.S. Wang, V.M. Schmidt, J. Power Sources 141 (2005) 205–210.
[30] D.J.L. Bret, S. Atkins, N.P. Brandon, V. Vesovic, N. Vasileiadis, A.R. Kucernak, Electrochem. Commun. 3 (2001) 628–632.
[31] T. Zhou, H. Liu, in: Proceedings of the ASME, vol.1, Heat Transfer Division-2002, Florida, 2002, p.43–49.